Wave-induced chaotic radial transport of energetic electrons in a laboratory terrella experiment

H. P. Warren[a)] and M. E. Mauel

Department of Applied Physics, Columbia University, New York, New York 10027

This paper reports the observation of wave-induced chaotic radial transport of energetic electrons in a laboratory terrella, the Collisionless Terrella Experiment (CTX) [H. P. Warren and M. E. Mauel, Phys. Rev. Lett. **74**, 1351 (1995)]. Electron cyclotron resonance heating is used to create a localized population of energetic electrons which excite the hot electron interchange instability. The electrostatic fluctuations driven by this instability have time-evolving spectra which resonate with the precessional drift motion of the hot electrons. We have established that the amplitude, frequency, and azimuthal mode number of the observed instabilities meet the conditions for the onset of chaotic particle motion. Electron transport is observed with a gridded particle detector. Increases in the flux of energetic particles to the detector are well correlated with the presence of fluctuations which meet the conditions for global chaos. Greatly diminished transport is observed when the fluctuations lead to thin, radially localized bands of chaos. The flux of energetic electrons to the detector is strongly modulated. By examining time-dependent Hamiltonian phase space flows, the modulation is shown to be the result of phase space correlations. A transport simulation based on the Hamiltonian motion of energetic electrons reproduces the frequency and modulation depth of the observed electron flux and allows for comparison between the Hamiltonian and quasilinear descriptions of transport. © *1995 American Institute of Physics.*

I. INTRODUCTION

Chaotic radial transport plays a central role in the formation and evolution of energetic particle populations trapped in planetary magnetospheres. Of primary importance to models of the Earth's magnetosphere is transport driven by random variations in the solar wind intensity and the interplanetary magnetic field which couple to the Earth's geomagnetic and convection electric fields.[1] Sudden, large-scale variations which have a decay time on the order of a precessional drift period can lead to resonant wave-particle interactions and the breaking of the third adiabatic invariant, ψ. The resulting transport is an essential mechanism for both the injection of particles into the magnetosphere and their acceleration.[2]

The dynamics of energetic particle populations in the Earth's magnetosphere may be of practical importance. For example, sudden increases in relativistic electron fluxes associated with geomagnetic storms are thought to be responsible for the failure of electronic components on spacecraft.[3,4] It has also been suggested that the precipitation of relativistic electrons can affect levels of stratospheric ozone by creating hydrogen and nitrogen oxides which catalytically destroy ozone.[5]

Quasilinear models have been used to account for the radial profile of radiation belt particles measured with satellites[6,7] as well as the stormtime enhancement and quiet time evolution of ring current particles.[8–10] Quasilinear theory is, however, only an approximate statistical description of many transport processes. Phase space structures often persist even in the presence of symmetry-breaking perturbations and the dispersion predicted by quasilinear theory is not observed.[11] Even when phase space is almost completely stochastic, deviations from quasilinear theory are possible.[12] This is especially relevant to many physically realized situations where the conditions necessary for the validity of quasilinear theory are not strictly met.

A more complete description of particle transport is given by the guiding center drift Hamiltonian.[13,14] The chaotic radial transport of ring current protons driven by magnetospheric hydrodynamic waves has been examined by Chan, Chen, and White[15] using Hamiltonian methods. For spectra characterized by multiple discrete modes, the extent of the transport is restricted both in radius and in energy by the existence of specific wave-particle resonances. A Hamiltonian approach has also been used to model the enhancement of ring current protons due to impulsive stormtime variations in the Earth's convection electric field by Chen *et al.*[16–18]

In an earlier paper,[19] we reported the first observation of wave-induced chaotic radial transport in a laboratory terrella experiment, the Collisionless Terrella Experiment (CTX). One of the primary goals of CTX is to study the process of chaotic radial transport in dipole magnetic fields. In particular, these experiments investigate the relationship between fluctuation spectra and models of energetic particle transport and provide the first laboratory tests of Hamiltonian methods which can be used to simulate magnetospheric transport. This paper presents a more complete description of the experimental observations and reports the detailed results of numerical simulations which model transport processes observed in the experiment.

In CTX, an energetic population of trapped electrons is produced using electron cyclotron resonance heating (ECRH).[20] The trapped electrons excite quasiperiodic "bursts" of drift-resonant electrostatic fluctuations which we identify as the hot electron interchange instability.[21,22] Al-

---

though the hot electron interchange instability is not excited naturally in planetary magnetospheres, the process by which nonaxisymmetric fluctuations induce chaotic radial transport of collisionless, trapped particles is independent of wave dispersion characteristics. Instead, chaotic radial transport occurs only when the spectral and spatial characteristics of the fluctuations meet specific requirements, and these requirements are documented in the laboratory using the hot electron interchange mode. We note further that the drift-resonant fluctuations drive strongly chaotic radial motion which preserves the first two adiabatic invariants μ and J.[23] Thus the experimentally observed transport processes are relevant to magnetically trapped magnetospheric particles drift-resonant with fluctuations which have low azimuthal mode numbers.

By computing Poincaré surfaces of section we find that during the instability bursts the measured amplitudes, frequencies, and azimuthal mode numbers of the drift-resonant fluctuations meet the conditions required for global chaotic particle transport. During the instability bursts significantly enhanced electron transport is observed with a gridded particle detector. The observed transport is strongly modulated at frequencies related to the precessional drift-frequency of the energetic electrons. At other times, when the instability wave spectrum does not satisfy the conditions for global chaos, no enhanced transport is observed.

The Poincaré surfaces of section which model particle motion during the instability bursts show that phase space is strongly chaotic and indicate that quasilinear theory should be applicable. However, in order to model the spatial and temporal evolution of particle fluxes observed in the experiment, computer simulations using the guiding center drift Hamiltonian are necessary. The first of these simulations involves visualizing the Hamiltonian flow of phase space as a function of time so that the evolution of equatorial particle trajectories can be examined. By examining animations of phase space flows, the observed modulation in the electron flux can be understood in terms of phase-space correlations. The second simulation involves computing the flux of equatorial particle trajectories to a small region of phase space which represents the particle detector. This simulation reproduces the modulation depth and frequency of the experimentally observed electron flux. When the results of the Hamiltonian transport simulation are compared with a simple quasilinear transport model we find that the predictions of the quasilinear model do not reproduce the experimentally observed modulations and underestimate the maximum particle fluxes measured in the experiment.

An interesting aspect of the experimental measurements we report here is the complicated evolution of the frequency content of the observed fluctuations. Both at the end of a quasiperiodic burst and during the afterglow, when the conditions for global chaos are not met, the wave-frequency increases in time or "chirps." Such behavior is often exhibited by evolving nonlinear systems and is a topic important both to nonlinear dynamics in general and to specific transport studies in other magnetically confined plasmas.[24]

The Collisionless Terrella Experiment differs significantly from previous terrella experiments designed to study
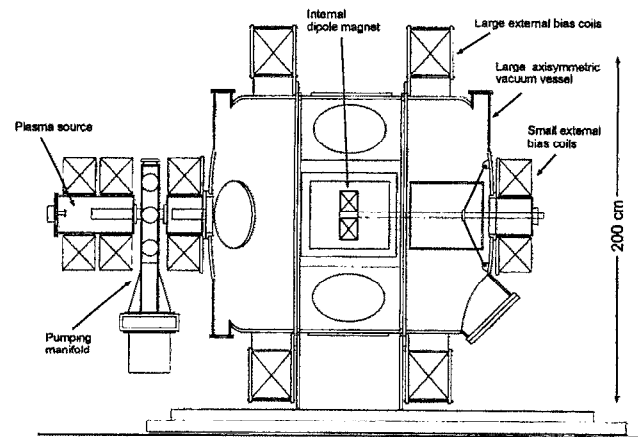

FIG. 1. A schematic diagram of the Collisionless Terrella Experiment showing the vacuum vessel and the dipole magnet.

the interaction of a steady solar wind with the geomagnetic field.[25] For these experiments, the CTX device employed only a pure dipole magnetic field. CTX does not have a "simulated" solar wind and magnetic field coils that can be used to create a quasimagnetopause were not used. The plasmas produced in CTX are low-density, hot electron plasmas which do not have the same magnetohydrodynamic properties as those used to study the solar wind. The experiments reported here also differ from the "collisionless" terrella experiments conducted in ultra-high vacuum by Il'in and Il'ina.[26,27] They demonstrated the breakdown of the first two adiabatic invariants at high energy and observed a reduced adiabatic limit during the application of axisymmetric perturbations.

This paper is organized in the following manner. A description of the experimental device and the plasma diagnostics is given in Sec. II. The results of the experiments related to the observation of hot electron plasmas, drift-resonant fluctuations, and chaotic radial transport are given in Sec. III. The results of computer simulations which model the resulting phase-space topology using Poincaré surfaces of section, the evolution of Hamiltonian phase space flows, and the flux of energetic electrons to the particle detector are given in Sec. IV. Finally, a summary and discussion of the results are given in Sec. V.

II. THE COLLISIONLESS TERRELLA EXPERIMENT

The CTX experimental device consists of a dipole electromagnet suspended mechanically in an axisymmetric aluminum vacuum vessel 1.9 cm thick and 137 cm in diameter. As shown in Fig. 1, the magnet is supported by a stainless steel casing which houses the electrical and cooling leads. The strength of the dipole magnetic field is approximately 15 kG at the face of the magnet and falls off to less than 50 G at the wall. The magnetic field lines and mod-B surfaces of the dipole magnet used in CTX and are shown in Fig. 2.

Plasmas are created by breaking down and heating hydrogen gas using microwaves which resonate with the electron gyromotion (this is electron cyclotron resonance heating or ECRH). The microwave source is a continuous wave mag-
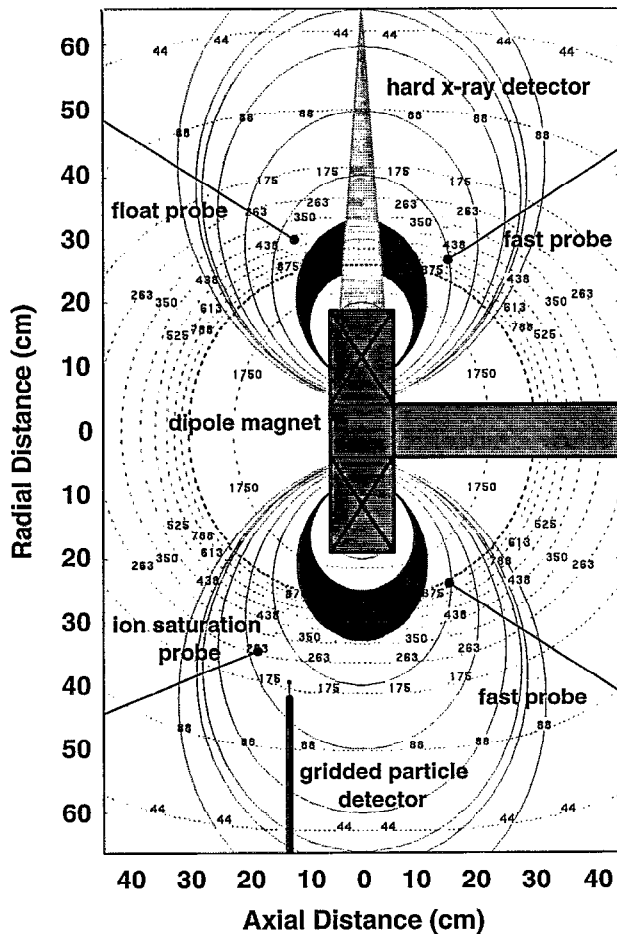
H. P. Warren and M. E. Mauel

FIG. 2. The magnetic field geometry of CTX. The solid lines represent magnetic field lines and the dotted lines represent surfaces of constant magnetic field. The location of several plasma diagnostics and the approximate location of the hot electron ring are also shown.

netron which has a peak output of 1500 W at a frequency of 2.45GHz. The rate of heating is proportional to the amount of time that an individual electron is resonant with a wave and the heating will be strongest for particles mirroring along the surface defined by $B_0 \equiv B \simeq 875$ G. The equatorial field strength of the dipole magnet has this value at a radial distance of $R_0 \equiv R \simeq 27$ cm and this defines the center of the hot electron "ring" or "artificial radiation belt."

Plasma diagnostics include a series of Langmuir and high impedance floating potential probes situated at five locations throughout the vacuum vessel. The probes can be repositioned radially to examine the density and potential fluctuations at different flux surfaces. Multiple probe measurements allow the direction of propagation, the azimuthal mode number and radial mode structure of the observed fluctuations to be determined. Data from the electrostatic probes are digitized using 8-bit, high-speed transient recorders which are capable of storing 2^{17} samples at rates of up to 100 million samples per second.

A krypton proportional counter is positioned at the midplane of the magnetic field and is used to measure hard x-ray emission at energies between 1–60 keV. The counter is col-

limated to view the equatorial region of the dipole magnetic field. X-ray spectra are collected and stored at 50 ms intervals during the plasma discharge using a multichannel analyzer and a histogramming memory unit.

A movable gridded particle detector is located inside the vacuum chamber 13 cm above the equatorial midplane. The particle detector is supported by a metal rod which extends from the vacuum chamber wall and can be repositioned to measure particle flux at different radial positions. The detector consists of a small square metal box 1 cm on a side with a 0.23 cm^2 opening centered on one face. The box contains a series of grids which are biased to repel ions and electrons with energies less than 100 eV.

The entrance aperture of the probe can be rotated with respect to the local magnetic field vector. For the measurements described here, the entrance was oriented perpendicular to the magnetic field. Gryoradius effects determine the minimum particle energy detected by the probe. The minimum detectable energy ranges from 700 eV to 2.3 keV depending on the radial position of the probe. Since the probe is located above the midplane of the magnetic field, only particles with a sufficiently small equatorial pitch angle will be detected by the particle detector. The maximum pitch angle ranges from 54° to 65°.

III. EXPERIMENTAL OBSERVATIONS

The operation of the Collisionless Terrella Experiment is relatively simple. After the dipole electromagnet is turned on, hydrogen gas is puffed into the vacuum chamber and heated with microwaves. After a specified time the microwave power is turned off and the hot electron "afterglow" of the plasma discharge can be examined. Computer controlled timing signals define intervals when the high speed transient recorders store diagnostic signals.

A. Characterization of hot electron plasmas

The intensity of the hot electron population is characterized by the hard x-ray emission produced by electron-ion and electron-neutral bremsstralung. A fraction of these x-rays are detected with the krypton proportional counter. The measured x-ray spectra indicate the formation of a magnetically trapped, energetic electron population with energies between 1–60 keV. The observed distributions are non-Maxwellian and more closely resemble power-law distributions often associated with wave-heated space plasmas.[28] There are two distinct subpopulations within the electron distribution. There is a "warm" population with energies between 1–10 keV, and a "hot" population, which is more sensitive to variations in background pressure, with energies above 10 keV.

As shown in Fig. 3, the distribution of energetic electrons is dependent on the hydrogen fill pressure. Whenever the peak pressure falls either above or below the optimal value the hot electron population is reduced. A similar dependence of hot electron intensity on background pressure has been reported in other ECR heated magnetic mirror experiments.[29]

The spatial extent of the energetic electron population is established by using a Langmuir probe as a "limiter" or "skimmer" and moving it into the resonance region until the
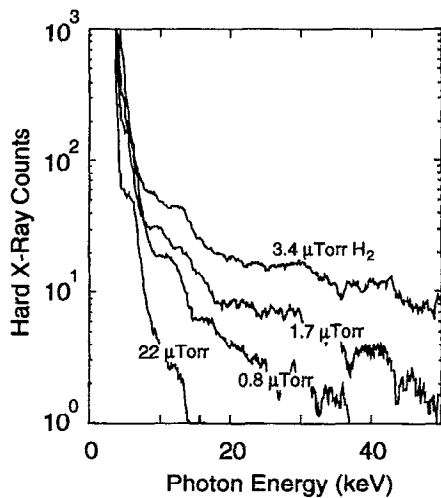
FIG. 3. Hard x-ray emission as a function of hydrogen fill pressure. If the peak pressure falls above or below the optimal value, the hot electron energy will be reduced.
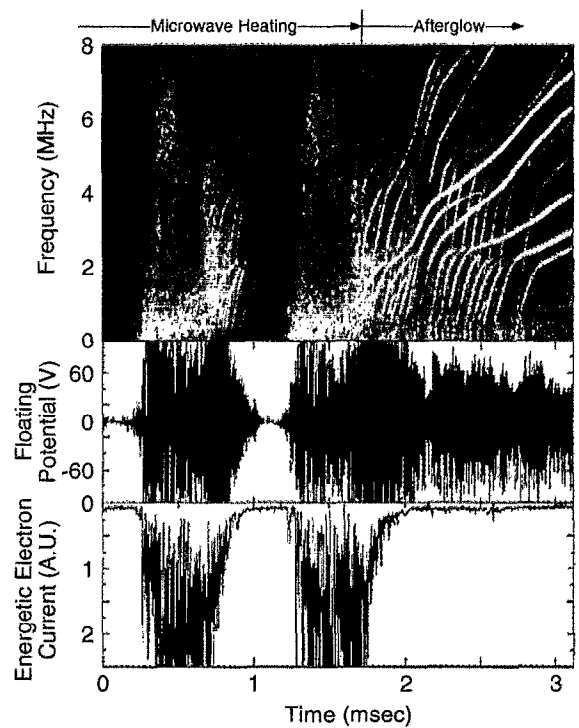

FIG. 4. The flux of energetic electrons to the gridded particle detector, the measured floating potential, and a color contour plot of the corresponding spectrogram. The observation of transport with the particle detector is correlated with the presence of fluctuations which satisfy the conditions for global chaos. The measurements begin during the ECRH phase and extend into the afterglow of the plasma discharge.
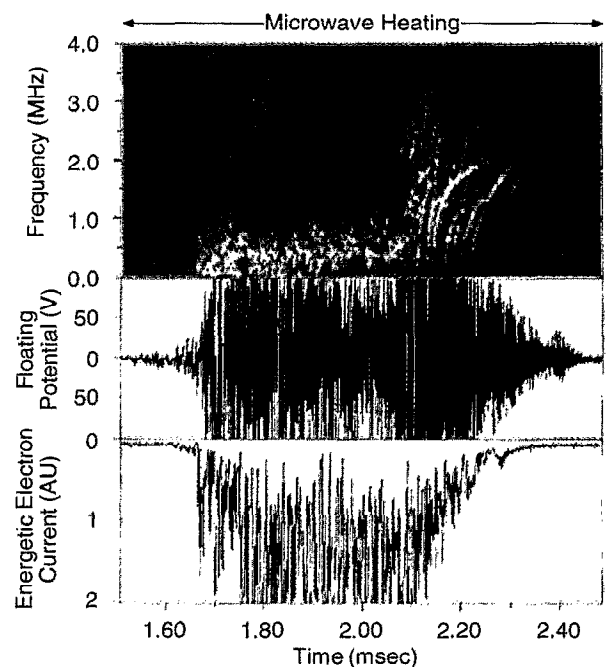
x-ray emission is significantly diminished. Plasmas without a significant hot electron population can also be created by decreasing the dipole's magnetic field. When the field strength is sufficiently small, the resonant surface coincides with the surface of the magnet and no hard x-ray emission is observed.

B. Observation of drift-resonant fluctuations

When a sufficiently intense hot electron population is present, electrostatic fluctuations which resonate with the precessional drift-motion of the hot electrons ($\omega \sim \omega_{dh}$) are detected by the Langmuir probes. Fluctuations are observed both while the ECR heating is on and in the afterglow of the plasma discharge, when the heating has been turned off.

While the ECR heating is on, quasiperiodic bursts of drift-resonant fluctuations with a growth rate of ~ 50 μs and which last approximately 300–700 μs are observed. The rate at which the instability bursts appear is a strong function of the hot electron energy: at the highest observed energies the bursts become almost continuous, at lower energies the time between bursts increases to intervals as long as several milliseconds. During the afterglow, the observed fluctuations have a slower growth rate, ~ 100 μs, and persist for several milliseconds.

During both the ECRH and in the afterglow, the observed instabilities propagate azimuthally in the direction of the curvature and ∇B drift motions of the electrons. The observed instabilities are flute modes with no structure along a field line and have only a weak radial dependence. The saturated wave amplitudes observed during both the ECRH and the afterglow are also similar, typically 100–200 V, with the larger amplitudes resulting from the most energetic electron populations.

The time evolution of the frequency content of the observed fluctuations can be examined by computing the time-frequency domain (TFD) of the Langmuir probe signals. One of the simplest and most intuitive algorithms for computing the TFD is the short-time Fourier transform or

FIG. 5. A detailed spectrogram of the first instability burst shown in 4. For the first 450 μs of the burst the fluctuations are incoherent and resonate with the "warm" part of the energetic particle population and enhanced transport is observed. For the final 200 μs the fluctuations are more coherent, the instability "chirps" upward in frequency, and the transport is diminished.

H. P. Warren and M. E. Mauel

spectrogram.[30] An example of a discharge in which drift-resonant fluctuations have been observed is shown in Fig. 4 where a floating potential probe signal and its spectrogram are displayed. The measurement was taken at the end of the heating phase and extends into the afterglow. This Fourier analysis indicates that the quasiperiodic bursts consist of incoherent, broad-band fluctuations with frequencies typically below 2 MHz, although some particularly intense bursts have frequencies as high as 5 MHz. The instabilities observed during the afterglow are more coherent than those observed during the ECRH and have a higher range of frequencies, $f \sim 1-12$ MHz.

Inspection of the spectrogram shown in Fig. 4 reveals that the wave frequency evolves in a very complicated way both during the ECRH and in the afterglow. Fig. 5 shows the spectrogram of a single burst in detail and it is clearly seen that the quasiperiodic fluctuations consist of two different stages. During the initial stage of the burst, lasting 300 μsec, the fluctuations have frequencies below 1 MHz and appear to be incoherent. At the end of the burst, the fluctuations become more coherent and rapidly increase in frequency or "chirp." During the afterglow only coherent, rising tone fluctuations are observed.

The fluctuations observed during the ECRH also differ from those observed in the afterglow in terms of their azimuthal mode number. During the quasiperiodic instability bursts, the azimuthal mode number is usually limited to $m=1$, except in the most intense bursts when some high-frequency, $m=2$ modes are observed. In the afterglow, $m \lesssim 6$, and there are often multiple waves with the same azimuthal mode number present simultaneously.

The drift-resonant fluctuations observed in the experiment are related to the hot electron interchange instability that has been observed in other ECR heated magnetic mirror experiments.[31,32] The linear theory of the hot electron interchange, assuming slab geometry and a monoenergetic distribution of electrons, was developed by Krall for $\omega \ll \omega_{ci}$[21] and by Berk[22] for $\omega \sim \omega_{ci}$ and the observed fluctuations are generally similar to those predicted by these simple theories.

C. Observation of energetic electron transport

Coincident with the bursts of wave activity observed during the ECRH are increases in the flux of energetic electrons to the gridded particle detector. The characteristics of the transport measurements suggest a definite relationship between the spectral content of the waves and the observed energetic particle flux. As shown in both Fig. 4 and Fig. 5, the electron current rises significantly above the background level during the low-frequency, incoherent phase of the quasiperiodic bursts. Transport is diminished during the coherent phase of a burst when the frequency of the instability "chirps" upward. No enhanced transport is associated with the high-frequency, coherent modes observed during the afterglow. Also note that the observed energetic electron flux is strongly modulated at frequencies related to the precessional drift-frequency of the "warm" electrons. The connection between the fluctuation spectrum and energetic electron transport will be examined in detail in the next section.

IV. WAVE-INDUCED PARTICLE TRANSPORT

The interaction of energetic electrons with the drift-resonant electrostatic waves observed in the experiment can be described by the guiding center drift Hamiltonian[14]:

$$\mathscr{H} = \frac{m_e c}{2e} \rho_{\parallel}^2 B^2 + \mu \frac{cB}{e} - c\Phi, \tag{1}$$

where m_e and e are the electron mass and charge, c is the speed of light, B is the magnitude of the dipole magnetic field, $\mu \equiv m v_{\perp}^2 / 2B$ is the magnetic moment, $\rho_{\parallel} \equiv v_{\parallel}/B$, and Φ is the electrostatic potential. For a curl-free magnetic field, the canonical coordinates of the guiding center drift Hamiltonian, $(\rho_{\parallel}, \chi)$, and (ψ, φ), are essentially the magnetic coordinates defined by: $\mathbf{B} = \nabla \psi \times \nabla \varphi = \nabla \chi$. The function $\psi = M \sin^2 \theta / r$ is proportional to the magnetic flux bounded by a field line and the function $\chi = M \cos \theta / r^2$ is related to the distance along a field line. Note that $M \equiv B_0 R_0^3$ is the moment of the dipole magnet and (r, φ, θ) are spherical coordinates. Also note that the guiding center drift Hamiltonian is appropriate since energetic electrons produced in the experiment are nonrelativistic.

When the particle motion is confined to the equatorial midplane of the magnetic field, $\rho_{\parallel} = \chi = 0$, $B = B(\psi)$, and the equations of motion are reduced to a particularly simple form:

$$\frac{d\psi}{dt} = -\frac{\partial \mathscr{H}}{\partial \varphi} = c \frac{\partial \Phi}{\partial \varphi},$$

$$\frac{d\varphi}{dt} = \frac{\partial \mathscr{H}}{\partial \psi} = \mu \frac{c}{e} \frac{\partial B}{\partial \psi} - c \frac{\partial \Phi}{\partial \psi}. \tag{2}$$

These are the equations that will be considered in this paper. For equatorial particles the precessional drift frequency is:

$$\omega_{dh} = \frac{3c\mu B}{e\psi} = \frac{3\mu B_0}{m_e \Omega_0 R^2}, \tag{3}$$

where $\Omega_0 = eB_0/m_e c$ and R is the particle's radial position. In general, particles will have a finite parallel velocity and will not be confined to the equatorial midplane. However, the precessional drift-frequency is only weakly dependent on pitch angle[2] and the results presented here would not be significantly altered by including parallel velocity.

The experimental observations described in the previous section indicate that the observed fluctuations can be modeled as a sum of traveling waves of the form:

$$\Phi(\varphi,t) = \frac{\Phi_0}{\sqrt{\mathscr{S}}} \sum_{m,l}^{N} a_{ml} \cos(m\varphi - \omega_l t + \varphi_l), \tag{4}$$

where $\mathscr{S} = \Sigma_{ml} |a_{ml}|^2$. The relative amplitudes, azimuthal mode numbers, frequencies, and phases are determined from the Fourier analysis of experimentally measured Langmuir probe signals.

For a single electrostatic wave the island half-width, $\Delta \psi$, at the resonant surface defined by $\omega_l - m\omega_{dh}(\mu, \psi_{lm}^r) = 0$, is given by the solution to the equation:

$$(\Delta \psi)^2 \left[1 + \frac{\Delta \psi}{3\psi_{lm}^r} \right] - \frac{2c\Phi_0 \psi_{lm}^r}{\omega_{dh}} = 0. \tag{5}$$
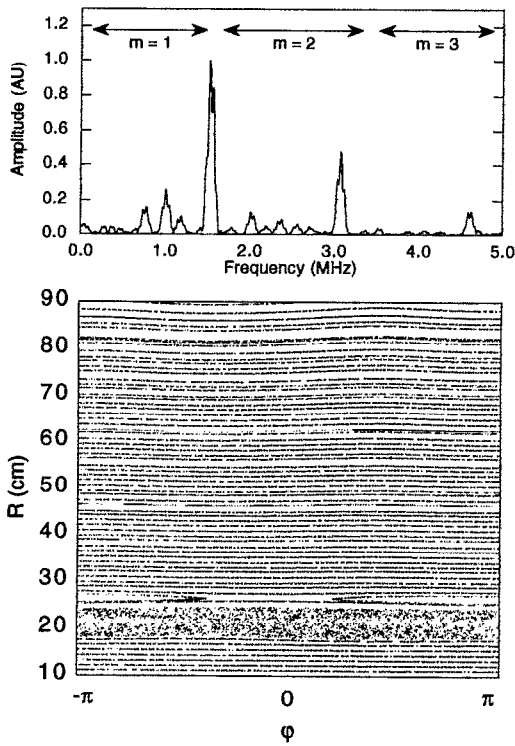
FIG. 6. A spectrum of waves taken from experimental measurements of fluctuations observed during the afterglow and a corresponding Poincaré surface of section. The chaos is localized to a thin, radially localized band near the hot electron ring and consistent with the absence of electron flux to the particle detector. The magnetic moment, μ, is chosen so that $\mu B_0 = 10$ keV; other parameters are $\Phi_0 = 150$ V, $N = 10$, and $T_M = 100$ μs. Note that the surface of section is plotted in (R, φ) coordinates.
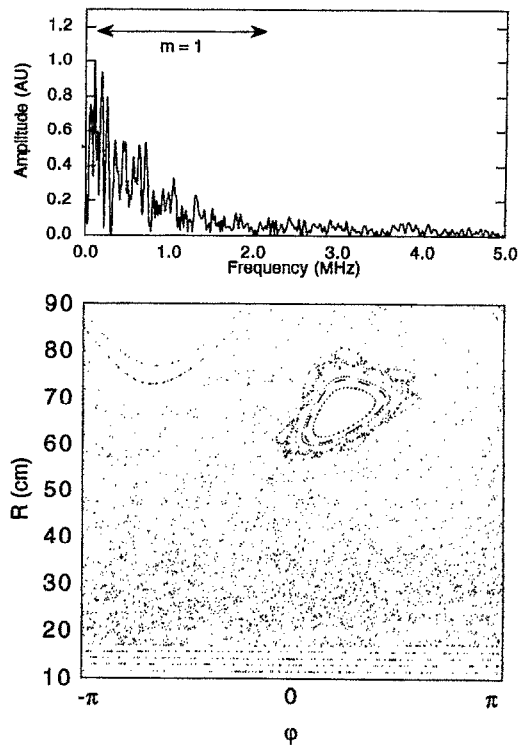

FIG. 7. A spectrum of waves taken from experimental measurements of fluctuations observed during the ECRH and a corresponding Poincaré surface of section. The fluctuations spectrum leads to chaos in ψ over the radial extent of the plasma. The magnetic moment, μ, is chosen so that $\mu B_0 = 4$ keV; other parameters are $\Phi_0 = 150$ V, $N = 10$, and $T_M = 100$ μs. Note that the surface of section is plotted in (R, φ) coordinates.

When the islands are small they are approximately symmetric and the island half-width is given by $\Delta \psi \approx (2c\Phi_0 \psi^r_{lm}/\omega_{dh})^{1/2}$. When multiple drift-resonant waves with sufficiently large amplitude are present, islands will overlap and lead to chaotic transport.

The topological properties of particle trajectories can be determined by constructing the Poincaré surface of section which is formed by plotting (ψ, φ) at multiples of the mapping time. For a spectrum of waves, the mapping time is the least common multiple of the periods of the wave motion: $T_M = \text{LCM}(T_l = 2\pi/\omega_l)$.[33] In practice, the frequencies are rounded off to keep T_M from becoming too large. The equations of motion are integrated using the Gragg-Burlish-Stoer implementation of the Richardson extrapolation.[34]

A. Chaos during the afterglow

An example of a fluctuation spectrum used to model the electrostatic potential observed during the afterglow is shown in Fig. 6a. For electrons with energies above $\mu B_0 \approx 10$ keV this spectrum leads to resonant wave-particle interactions. However, as the Poincaré surface of section shown in Fig. 6b illustrates, the thin bands of chaos in ψ are limited to the proximity of the hot electron ring and do not extend out to the radial location of the gridded particle detector unless the amplitude of the potential fluctuations is very large.

B. Chaos during the quasiperiodic bursts

A number of model fluctuation spectra have been constructed to model the potential fluctuations observed during the ECRH. For the wave spectrum shown in Fig. 7a, which is taken from the initial part of an instability burst, drift-resonances exist for electrons with energies between 1–10 keV (i.e., the "warm" electrons) from the center of the hot electron ring to the wall of the vacuum chamber. As shown in Fig. 7b, this spectrum of waves leads to chaos in ψ over the radial extent of the plasma. Examination of the phase space portraits indicates that when the wave amplitude is above ≈ 75 V, there are no encircling Kolmogorov-Arnol'd-Moser (KAM) surfaces[35] preventing global transport.

As shown in Fig. 5, the quasiperiodic bursts observed during the ECRH evolve into more coherent modes that rapidly chirp upward to higher frequencies. By the end of a burst these modes have begun to resemble modes observed in the afterglow. Coincident with the transition from incoherence to coherence, the observed particle flux to the detector begins to decline. This is understandable in light of the Poincaré surfaces of section shown in Fig. 6 and Fig. 7. The higher frequency waves lead to chaos that is confined to narrow regions of phase space. This observation also suggests that there is a complicated relationship between the frequency content of the instability, particle transport, and the coherence of the fluctuations.

H. P. Warren and M. E. Mauel

C. Hamiltonian phase space flows

The transport associated with the quasiperiodic bursts observed during the ECRH is strongly modulated. This type of behavior is suggestive of "drift echoes" which have been observed in satellite measurements of energetic particle transport.[36,37] Drift echoes result from the sudden injection of energetic particles at a narrow range of longitude. If the injected particles differ from the background population, each time they drift past the satellite a change in the particle flux is observed. As we will show, a similar process is responsible for the modulation of the observed particle flux in CTX. The particle motion in CTX is chaotic but the decorrelation time is long with respect to a drift period. Thus inhomogeneities in phase space propagate azimuthally and lead to temporal variations in the observed particle flux.

The Poincaré surface of section, while a useful way of obtaining topological information about phase space, does not provide sufficient information about the temporal evolution of particle trajectories to understand the modulation observed in the electron flux. The evolution of phase space, however, can be examined by computing the Hamiltonian phase space flow. For a $1\frac{1}{2}$ degree of freedom Hamiltonian, flows can be computed by dividing the (ψ,φ) plane into an $M \times M$ grid and evolving the equations of motion for each grid point. Since radial transport is of interest here, trajectories initially on the same radial flux surface are assigned the same color. In order to maintain a uniform distribution of grid points, the equations of motion are integrated backwards in time.

An example of a Hamiltonian phase space flow is shown in Fig. 8 where six "frames" from an animation of the phase space flow are displayed. The electrostatic potential used in the equations of motion is the same as was used to compute the Poincaré surface of section shown in Fig. 7. Clearly evident is the relatively slow, inhomogeneous mixing of phase space.

To understand how these pictures relate to the experimental observations, recall that the use of ECRH leads to a strong radial gradient in the hot electron density. The different colors used to identify a phase space element's initial radial position could also represent the initial particle density of the phase space element. Thus a consequence of the relatively slow mixing of phase space is that the density of particles reaching the detector has a very complicated time dependence. These simulations indicate that it is this process that is responsible for the modulation of the flux of electrons to the gridded particle detector observed in the experiment.

D. Hamiltonian transport simulation

In order to demonstrate the relationship between the chaotic mixing of phase space and the modulation of the energetic electron flux more directly, a numerical simulation which computes the time-evolution of the flux of energetic electrons to a small region of phase space has been performed. The objective of the simulation is to reproduce the gross frequency and amplitude of the modulation present in the observed energetic electron flux.

In the code, an ensemble of particle trajectories that are at the "gridded particle detector" at time $t = T$ are randomly selected. The values for ψ and φ are selected randomly from a region of phase space determined by the position and the area of the probe. As with the Poincaré surfaces of section and the Hamiltonian phase space flow, spectral information from the experiment is used to construct the electrostatic potential in the form of Eq. (4). However, in order to model the growth of the wave the spectrum is modified to include a time-dependent wave amplitude: $\Phi_0 \to \Phi_0(t) = \Phi_0 \tanh(\tau^2 t^2)$, where τ is the growth time of the fluctuations. To increase computational efficiency, the equations of motion are integrated backwards in time from $t = T$ to $t = 0$ rather than forward in time.

To model the finite extent of the experimental device, trajectories that move beyond the vacuum chamber wall, $R > R_w$, are considered lost. Particles may also be lost if they strike the metal column which extends from the wall to support the gridded particle detector or the detector itself. In the simulation, any trajectory which crosses the location of the probe, $R > R_d$ and $\varphi = \varphi_d$, has a finite probability of being removed.

At $t = 0$ the probability that a trajectory came from a model hot electron distribution, $F_h(\mu,\psi)$, is computed. The hot electron distribution is assumed to be of the form:

$$F_h(\mu,\psi,t=0) = N_h \alpha(\psi,t=0) f(\mu), \qquad (6)$$

where $N_h \equiv n_h V$ is the number of particles within a flux tube of volume V. The initial spatial dependence of the hot electron distribution is taken to be:

$$\alpha(\psi,t=0) = a(\psi/\psi_0 - \psi_d/\psi_0)^b (2 - \psi/\psi_0)^c, \qquad (7)$$

where $\psi_0 = B_0 R_0^2$ and $\psi_d = B_0 R_0^3/R_d$. Note that two of the three parameters a, b, and c are chosen so that $\alpha(\psi_0) = 1$ and $\alpha'(\psi_0) = 0$. The remaining parameter can be adjusted to change the steepness of the profile. The magnetic moment μ is chosen from an exponential distribution:

$$f(\mu) = \frac{1}{\mu_0} \exp(-\mu/\mu_0), \qquad (8)$$

To model the energy resolution of the probe, only trajectories with $\mu B_0 \in [E_{\min}, E_{\max}]$ are integrated.

If a trajectory is determined to have come from the hot electron ring, it is used to construct the current:

$$I = e n_h A \langle v \rangle = e n_h A \frac{1}{\mathcal{N}} \sum_{i=1}^{\mathcal{N}} v_i, \qquad (9)$$

where $\frac{1}{2} m_e v_i^2 = \mu_i B(\psi_d)$ for the ith particle and A is the area of the probe. This process is repeated to construct $I(t)$.

The result of one such simulation is presented in Fig. 9 where it is compared with the corresponding energetic electron flux measurement from the experiment. The simulation was run with a randomly selected ensemble of 5000 particle trajectories. Also shown in Fig. 9 is the Fourier transform of the simulated and measured electrostatic fluctuations as well as the Fourier transform of the simulated and measured energetic electron flux. The simulation successfully reproduces the frequency of the observed modulations as well as the relative amplitude. Since the phases of the measured waves
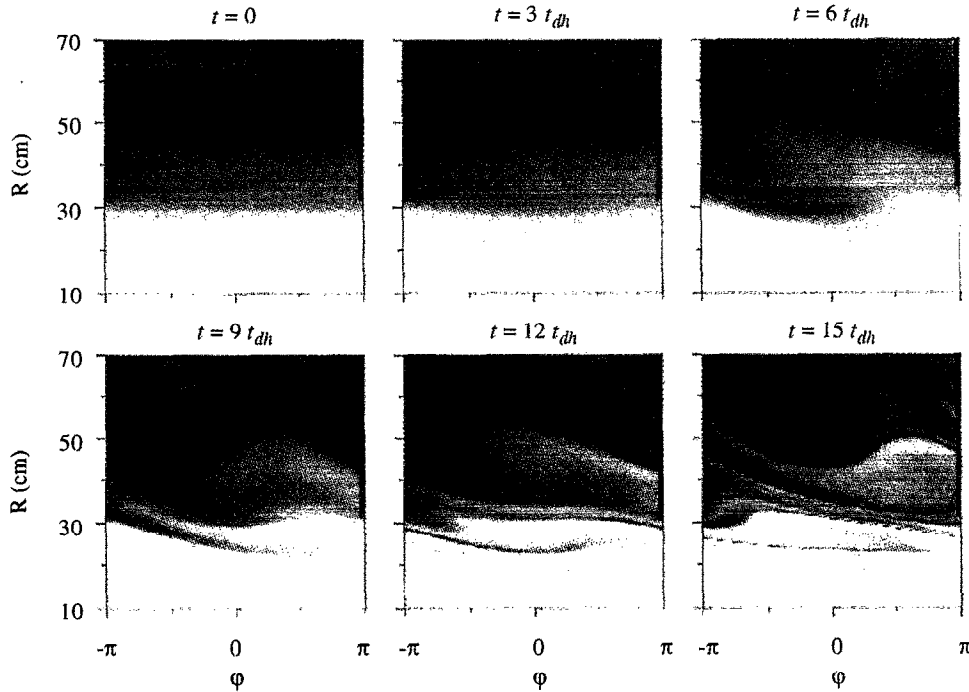
FIG. 8. Six "frames" from an animation of the Hamiltonian phase-space flow which show the slow, inhomogeneous mixing of phase space. The magnetic moment, μ, is chosen so that $\mu B_0 = 4$ keV ($t_{dh} = 3.34$ μs). $\tau = 10$ μs, $\Phi_0 = 150$ V and $M = 128$. Note that phase space is plotted in (R, φ) coordinates.

and other profile parameters are unknown, the simulation cannot be expected to reproduce the temporal evolution of the particle flux exactly.

E. Quasilinear transport simulation

In this section we explore the relationship between the Hamiltonian and quasilinear descriptions of chaotic particle transport. Quasilinear theory models transport as a random walk across flux surfaces with each step uncorrelated with the previous one. As is demonstrated by the phase space flows and the flux simulation, this does not describe the transport processes observed in the experiment. There are several reasons for this, the most important being that the measured fluctuation spectra have a finite bandwidth which allows particle trajectories to be correlated over several drift periods. Also, the fluctuation spectra may not lead to complete stochasticity. The presence of phase space structures, such as the islands shown in Fig. 7b, can increase the correlation time of particle trajectories.[11]

We have written a simple numerical simulation in order to compare the predictions of Hamiltonian and quasilinear descriptions of particle transport. In the code the simulated electron current is approximated by:

$$I(t) \approx eA \int d^3v\, v F_h(\mu, \psi_d, t) \sim eA n_0 \alpha(\psi_d, t) \langle v \rangle, \quad (10)$$

where $\langle v \rangle$ is the average velocity of particles reaching the detector. The function $\alpha(\psi, t)$ evolves according to a diffusion-like equation:

$$\frac{\partial \alpha}{\partial t} = \frac{\partial}{\partial \psi} \bar{D}_{\psi\psi} \frac{\partial \alpha}{\partial \psi} - \frac{\alpha}{t_L} \theta(\psi - \psi_d), \quad (11)$$

where $\bar{D}_{\psi\psi}$ is the diffusion coefficient averaged over resonant velocities. The second term in Eq. (11) models particle losses due to the probe and $\theta(\psi - \psi_d)$ is the unit step function. The boundary conditions are set so that the solution goes to zero at the wall and the magnet casing. The initial distribution for α is given by Eq. (7).

The quasilinear diffusion coefficient for the model fluctuation spectrum used in the Hamiltonian simulation [Eq. (4)] is given by:

$$D_{\psi\psi} = \frac{\pi m^2 c^2 \Phi_0^2}{2\mathscr{S}} \sum_{ml} |a_{ml}|^2 \delta(\omega_l - m\omega_{dh}(\mu, \psi)), \quad (12)$$

where $\delta(\omega_l - m\omega_{dh})$ is the Dirac delta function. The diffusion coefficient averaged over resonant velocities yields $\bar{D}_{\psi\psi}$. Alternatively, the diffusion coefficient can be determined from integrating the equations of motion as was done by Chen et al.[17] In this case the diffusion coefficient is computed using the formula:

$$\bar{D}_{\psi\psi} = \frac{\langle (\psi(t) - \psi(0))^2 \rangle}{2t} - \frac{\langle (\psi(t) - \psi(0)) \rangle^2}{2t}. \quad (13)$$

The agreement between these two approaches is generally good and the numerically determined value is used in the simulation.

The result of a single run representative of the quasilinear simulation is shown in Fig. 10 where it is compared with the result from the corresponding Hamiltonian simulation. Significantly, the predictions of the quasilinear model do not reproduce the experimentally observed modulations and underestimate the maximum particle fluxes measured in the experiment.
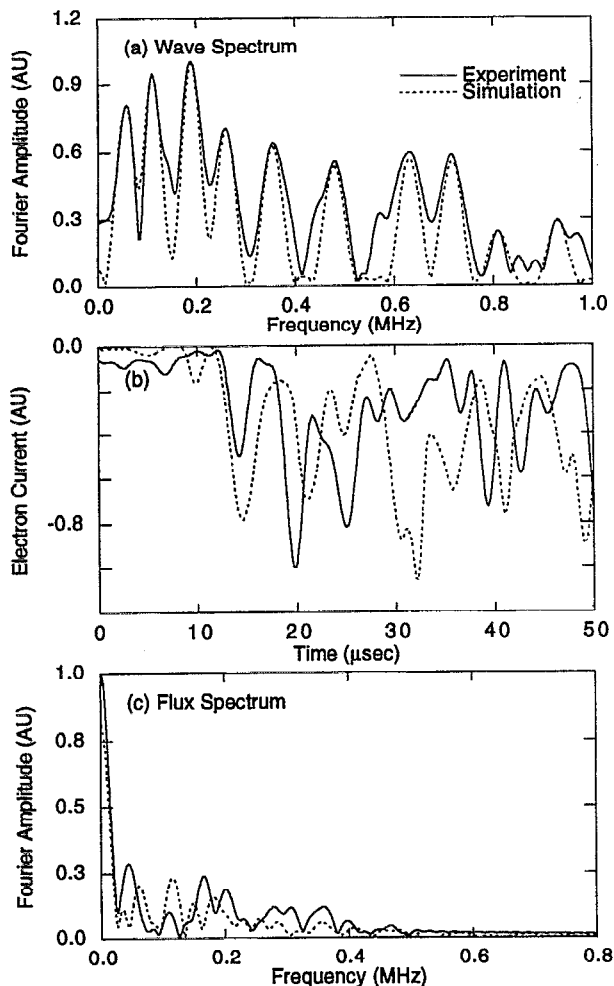
H. P. Warren and M. E. Mauel

FIG. 9. A comparison of experiment and a simulation which reproduces the gross frequency and depth of the modulation. (a) Frequency spectrum of the electrostatic waves, (b) detected energetic electron flux, and (c) Fourier transform of the detected flux.
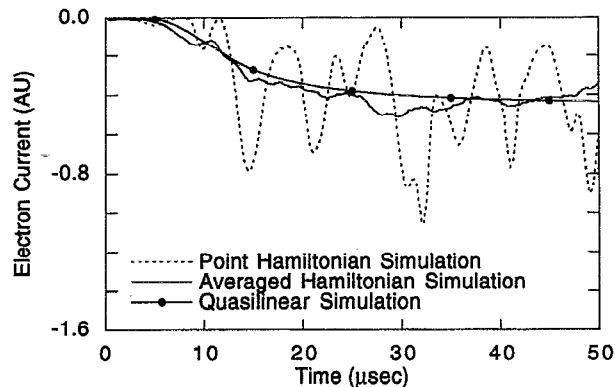
FIG. 10. A comparison of the energetic electron current computed from Hamiltonian and quasilinear models. The predictions of the quasilinear model lack the large-scale modulations seen in the experimental data and underestimate the maximum observed particle fluxes. There is, however, good agreement between the result of the Hamiltonian simulation averaged over a magnetic flux surface and the quasilinear simulation.

The failure of quasilinear theory to reproduce the salient features of the observed transport seems to be inconsistent with the strong chaos evident in the Poincaré surface of section shown in Fig. 7. We can reconcile this apparent discrepancy by considering the energetic electron flux predicted by the Hamiltonian simulation averaged over a magnetic flux surface. The result of such a calculation is presented in Fig. 10 where it is compared with the corresponding "point" result as well as the quasilinear result. The averaged energetic electron flux from the Hamiltonian simulation is very close to the quasilinear result indicating that the spatial resolution of the probe plays an important role in the deviations from quasilinear theory observed in the experiment.

V. SUMMARY

This paper reports the experimental observation of wave-induced chaotic radial transport of energetic electrons in a laboratory terrella. In the experiment ECRH is used to create a localized population of energetic, magnetically trapped electrons. The trapped electrons excite quasi-periodic, drift-resonant fluctuations which are identified as the hot electron interchange instability. Increases in the flux of energetic particles to a gridded particle detector are well correlated with the presence of the fluctuations. The measured particle flux is modulated at frequencies related to the precessional drift motion of the energetic electrons.

This paper has also presented the detailed results of numerical simulations based on the guiding center drift equations which model transport processes observed in the experiment. Most significantly, the simulations confirm that the observed transport is the result of nonlinear wave-particle interactions: transport is only observed when the wave-spectrum meets the conditions for global chaos; no transport is observed when the fluctuations lead to thin, radially localized bands of stochasticity.

The results of Hamiltonian simulations which explore the temporal details of the observed particle transport have also been presented. Animations of phase space flows have shown that the modulation of the flux of energetic electrons to the gridded particle detector can be understood in terms of the chaotic mixing of phase space. The relationship between chaotic mixing and the experimental measurements has also been demonstrated by a simulation which models the flux of energetic particles to a small region of phase space. The simulation reproduces the frequency and depth of the observed modulation. In contrast, quasilinear models of transport do not reproduce the modulation of the particle flux and underestimate the maximum particle fluxes observed in the experiment.

The results presented in this paper suggest that it may be worthwhile to model the temporal evolution of radiation belt particles in the magnetosphere using Hamiltonian methods. The results of such a study would better define the role that wave-induced chaotic radial transport plays in the dynamics of energetic particles in the magnetosphere. One candidate for driving drift-resonant chaotic radial transport similar to that observed in the experiment is low-m Pc 5 waves which have periods of 150–600 s. These ultra-low-frequency waves would drift-resonate with electrons with energies of 4–60

MeV at geosynchronous orbit and thus are strongly relativistic. Drift-resonant protons at geosynchronous orbit would have energies between 1–5 MeV but would be nonrelativistic.

Finally, we recognize that impulsive perturbations are of primary interest in magnetospheric transport of energetic particles but we stress that the modeling techniques used in this paper are clearly not restricted to wave-like perturbations. As mentioned in the introduction, Chen et al.[17] have modeled stormtime ring current proton enhancement due to impulsive variations in the Earth's convection electric field using the guiding center drift equations. They compared the dispersion averaged over a magnetic flux surface with the predictions of quasilinear theory and agreement between the two approaches was generally good. However, our results suggest that the averaged dispersion may not accurately represent the temporal evolution of energetic particle fluxes in localized regions of phase space.

ACKNOWLEDGMENTS

[1] J. W. Dungey, Space Sci. Rev. 4, 199 (1964).
[2] M. Schulz and L. J. Lanzerotti, Particle Diffusion in the Radiation Belts, Physics and Chemistry in Space (Springer-Verlag, New York, 1974), Vol. 7.
[3] A. L. Vampola, J. Electrostat. 20, 3 (1987).
[4] D. N. Baker, J. B. Blake, L. B. Callis, J. R. Cummings, D. Hovestadt, S. Kanekal, B. Klecker, R. A. Mewaldt, and R. D. Zwickl, Geophys. Res. Lett. 21, 409 (1994).
[5] R. M. Thorne, Pure Appl. Geophys. 118, 128 (1980).
[6] M. P. Nakada and G. D. Mead, J. Geophys. Res. 70, 4777 (1965).
[7] T. A. Farley, A. D. Tomassain, and M. Walt, Phys. Rev. Lett. 25, 47 (1970).
[8] C. G. Fälthammar, J. Geophys. Res. 70, 1487 (1965).
[9] W. H. Spjeldvik, J. Geophys. Res. 82, 2801 (1977).
[10] R. B. Sheldon and D. C. Hamilton, J. Geophys. Res. 98, 13491 (1993).
[11] G. M. Zaslavsky, D. Stevens, and H. Weitzner, Phys. Rev. E 48, 1683 (1993).
[12] A. B. Rechester and R. B. White, Phys. Rev. Lett. 44, 1586 (1980).
[13] R. G. Littlejohn, Phys. Fluids 20, 2445 (1979).
[14] A. H. Boozer, Phys. Fluids 23, 904 (1980).
[15] A. A. Chan, L. Chen, and R. B. White, Geophys. Res. Lett. 16, 1133 (1989).
[16] M. W. Chen, M. Schulz, L. R. Lyons, and D. G. Gorney, Geophys. Res. Lett. 98, 621 (1992).
[17] M. W. Chen, M. Schulz, L. R. Lyons, and D. G. Gorney, J. Geophys. Res. 98, 3835 (1993).
[18] M. W. Chen, L. R. Lyons, and M. Schulz, J. Geophys. Res. 99, 5745 (1994).
[19] H. P. Warren and M. E. Mauel, Phys. Rev. Lett. 74, 1351 (1995).
[20] M. Mauel, H. P. Warren, and A. Hasegawa, IEEE Trans. Plasma Sci. PS-20, 626 (1992).
[21] N. A. Krall, Phys. Fluids 9, 820 (1966).
[22] H. L. Berk, Phys. Fluids 19, 1255 (1976).
[23] H. P. Warren, A. Bhattacharjee, and M. E. Mauel, Geophys. Res. Lett. 19, 941 (1992).
[24] C. T. Hsu, C. Z. Cheng, P. Helander, D. J. Sigmar, and R. White, Phys. Rev. Lett. 72, 2503 (1994).
[25] K. Schindler, Rev. Geophys. 7, 51 (1969).
[26] V. D. Il'in and A. N. Il'ina, Sov. Phys. JETP 43, 661 (1976).
[27] V. D. Il'in and A. N. Il'ina, Sov. Phys. JETP 45, 514 (1977).
[28] V. Vasyliunas, J. Geophys. Res. 73, 2839 (1968).
[29] R. C. Garner, M. E. Mauel, S. A. Hokin, R. S. Post, and D. L. Smatlak, Phys. Fluids B 2, 242 (1990).
[30] S. H. Nawab and T. F. Quatieri, in Advanced Topics in Signal Processing, edited by J. S. Lim and A. V. Oppenheim (Prentice–Hall, Englewood Cliffs, NJ, 1988), pp. 289–337.
[31] S. Hiroe, J. B. Wilgin, F. W. Baity, L. A. Berry, R. J. Colchin, W. A. Davis, A. M. El Nadi, G. R. Haste, D. L. Hillis, D. A. Spong, and T. Uckan, Phys. Fluids 27, 1019 (1984).
[32] M. J. Gerver and B. G. Lane, Phys. Fluids 29, 2214 (1986).
[33] A. G. Kornienko, M. Y. Natenzon, R. Z. Sagdeev, and G. M. Zaslavsky, Phys. Lett. A 158, 398 (1991).
[34] W. H. Press, B. P. Flannery, S. A. Teukolsky, and W. T. Vetterling, Numerical Recipes: The Art of Scientific Computing (Cambridge University Press, Cambridge, 1986).
[35] A. J. Lichtenberg and M. A. Lieberman, Regular and Stochastic Motion, Applied Mathematical Sciences (Springer-Verlag, New York, 1983).
[36] L. J. Lanzerotti, C. S. Roberts, and W. L. Brown, J. Geophys. Res. 72, 5893 (1967).
[37] A. L. Vampola and A. Korth, Geophys. Res. Lett. 19, 625 (1992).